Remote Floating-Gate Field-effect Transistor with 2-Dimensional Reduced Graphene Oxide Sensing Layer for Reliable Detection of SARS-CoV-2 Spike Proteins

Hyun-June Jang[1,2], Xiaoyu Sui[1,2], Wen Zhuang[1], Xiaodan Huang[1], Min Chen[1], Xiaolei Cai[1], Yale Wang[3], Byunghoon Ryu[2], Haihui Pu[1,2], Nicholas Ankenbruck[1], Kathleen Beavis[4], Jun Huang[1], Junhong Chen[1,2*]

[1]Pritzker School of Molecular Engineering, University of Chicago, Chicago, IL 60637, USA

[2]Chemical Sciences and Engineering Division, Physical Sciences and Engineering Directorate, Argonne National Laboratory, Lemont, IL 60439, USA

[3]Department of Mechanical Engineering, University of Wisconsin-Milwaukee, Milwaukee, WI 53211, USA

[4]Department of Pathology, University of Chicago, Chicago, IL 60637, USA

Corresponding author

*E-mail: junhongchen@uchicago.edu

Abstract

Despite intensive research of nanomaterials-based field-effect transistors (FETs) as a rapid diagnostic tool, it remains to be seen for FET sensors to be used for clinical applications due to a lack of stability, reliability, reproducibility, and scalability for mass production. Herein, we propose a remote floating-gate (RFG) FET configuration to eliminate device-to-device variations of two-dimensional reduced graphene oxide (rGO) sensing surfaces and most of the instability at the solution interface. Also, critical mechanistic factors behind the electrochemical instability of rGO such as severe drift and hysteresis were identified through extensive studies on rGO-solution interfaces varied by rGO thickness, coverage, and reduction temperature. rGO surfaces in our RFGFET structure displayed a Nernstian response of 54 mV/pH (from pH2 to 11) with a 90% yield (9 samples out of total 10), coefficient of variation (CV) < 3%, and a low drift rate of 2%, all of which were calculated from the absolute measurement values. As proof-of-concept, we demonstrated highly reliable, reproducible, and label-free detection of spike proteins of severe acute respiratory syndrome coronavirus 2 (SARS-CoV-2) in a saliva-relevant media with concentrations ranging from 500 fg/ml to 5 μg/ml, with an R^2 value of 0.984 and CV < 3%, with a guaranteed limit of detection at a few pg/ml. Taken together, this new platform may have an immense effect on positioning FET bioelectronics in a clinical setting for detecting SARS-CoV-2.

Keywords: SARS-CoV-2 biosensor, graphene oxides, RFGFET, drift, pH detection

Introduction

The outbreak of coronavirus 2019 (COVID-19),[1] resulting from severe acute respiratory syndrome coronavirus 2 (SARS-CoV-2), has evolved into a global pandemic, causing more than 400 million infections and more than four million deaths (https://covid19.who.int/). The development of a reliable mechanism to track infectious diseases and their spread remains a challenge. Indeed, the early identification and diagnosis of potential pathogens is essential for preventing virus transmission.[2] The real-time reverse transcriptase polymerase chain reaction (RT-PCR) technique has been the gold standard for COVID-19 detection, but it can take hours to days to receive test results, as RT-PCR requires a large laboratory space, multistep sample preparation, and trained experts to perform the tests.[3] In contrast, several point-of-care (POC) testing tools based on lateral flow immunoassays (LFAs)[4] were recently authorized by the U.S. Food and Drug Administration (FDA) for emergency use, which are still inadequate to precisely identify a particular phase of COVID-19 disease progression in patients.

Meanwhile, proof-of-concept field-effect transistors (FETs) have been demonstrated for COVID-19 detection using nanostructured materials such as carbon nanotubes,[5] graphene,[6] reduced graphene oxide (rGO),[7] and transition metal dichalcogenide monolayers[8]. Those FET sensors eliminate the multiple laboratory steps that are typically required to amplify DNA sequence or immobilize the specialized reagents or enzymatic labels, as demanded by LFAs, conventional fluorescence, luminescence, and radioactive assays. A few reports on two-dimensional (2D) FETs have already shown excessively low limit of detection (LOD) for SARS-CoV-2 spike proteins (S proteins) down to 1 fg/ml[6], while the LOD observed from the conventional LFAs is measured as 5 ug/ml in literature[9], and capacities to screen SARS-CoV-2 in patient specimens.[6-7] However, to the best of our knowledge, none of FET sensors above has been authorized by FDA for emergency use or commercialized for clinical uses so far while most of impressive work has been shown for a single device scale accompanied with well-controlled laboratory environments for measurements.

A major technical hurdle of low-dimensional FET sensors[10-15] for POC market products is the lack of adequate control over the manufacturing quality for low-dimensional semiconducting layers.[16] As a result, electrical properties of low-dimensional materials easily fluctuate due to various factors such as grain boundaries, impurities, and defects, all of which if not adequately controlled over the fabrication process, could lead to random and inconsistent performance for the transducers.[17-20] Additional variation and instability could be introduced by directly placing a solution-gated system[21] on low-dimensional semiconducting layers as the gate; i.e., the nanomaterial plays a role of both sensing membrane and transducer. Inevitable interactions between the semiconducting layer and the media solution in terms of drain or gate current

flow cause degradation of the intrinsic electronic properties of nanomaterials through redox reactions and ion diffusion.[6, 22] Furthermore, physiological samples (i.e., saliva) add extra random factors in the measurement system such as different ionic concentrations, pH values, mucus, while blood cells, epithelial cells, and enzymes which could easily cause false or non-specific signaling of FET sensors. Thus, fundamental studies regarding device yield, stability, reliability, and reproducibility of low-dimensional materials are required for success of FET sensors toward rapid POC market products along with studies to achieve higher sensing performance.

It is well known that SARS-CoV-2 gains entry into target cells via an initial binding interaction between the S protein and the angiotensin-converting enzyme 2 (ACE 2) receptor on the host cell surface, followed by viral fusion and entry.[23] The S protein consists of a signal peptide, S1 subunit, S2 subunit, and transmembrane domain anchored in the viral membrane and expressed as a trimer. In the normal metastable, prefusion conformation of the S protein, the receptor-binding domain (RBD) of the S1 subunit is partially blocked, which prevents host cell entry. However, upon interaction with the host cell, proteases cleave the S protein into the S1 and S2 subunits, resulting in an open conformation that exposes the RBD and enables binding to ACE2. As the primary means for viral infection, the S protein is an ideal target for detecting SARS-CoV-2 in patients.

In this paper, we propose a new remote floating-gate (RFG) FET configuration (Figure 1a) with two-dimensional (2D) reduced graphene oxide (rGO) that eliminates non-reliable behaviors of solution interfacial properties for reliable and reproducible COVID-19 sensing applications. The rGO layer is electrically isolated by an insulator, while confining a 2D structure of the rGO layer only to the solution interface, and capacitively connected to the gate of FET transducer. The proposed structure blocks any current flows into rGO which avoids any undesirable effects from interface traps, defects, and redox reactions. As a result, highly uniform absolute levels of threshold voltage (V_{th}), i.e., intrinsic interfacial potentials of the rGO layer, are obtained for specific pH levels by the RFGFET. In addition, the rGO sensing membrane is highly sensitive to interfacial potential changes that are caused by protein binding on rGO layers due to the 2D structure of rGO isolated into solution interface with a high surface-to-volume ratio.

Using RFGFET platform, we first discovered critical mechanistic factors of rGO sensing layers behind drift and hysteresis in pH testing studies that were varied by device structure, rGO thickness, rGO coverage, and rGO reduction temperature. Our optimized rGO layer presented a Nernstian sensitivity of 54 mV/pH with an R^2 of 0.998 and a coefficient of variation (CV) < 3%, a 90% yield (9 samples out of total 10), a low drift rate of 2%, and no hysteresis, all of which are

directly calculated from a directly measured V_{th} of rGO for each pH. Also, this optimized rGO layer led to a reproducible sensitivity of SARS-CoV-2 S proteins (6.3 mV/dec) in the PBS buffer solution with a concentration range from 3.4 pg/ml to 34 ng/ml with an R^2 value of 0.986. Also, the sensitivity of S protein in a saliva-relevant media was measured to be 5.1 mV/dec in a range from 500 fg/ml to 5 μg/ml, with an R^2 value of 0.984 and CV < 3%, while the guaranteed LOD is at a few pg/ml. Taken together, this work provides a novel platform for POC testing of COVID-19 that is rapid, sensitive, selective, reproducible, and reliable.

Results and Discussion

Structural advantages of RFGFET. 4 nm-thickness multilayer rGO on a 300-nm-thick SiO_2 is capacitively coupled to the commercial FET transducer (**Figure 1a**). The 2D structure offered by the rGO layer is only confined to the solution interface on the FG by the SiO_2 insulator, which preserves the high surface-to-volume ratio for the sensing section. In contrast, it is challenging to avoid any influences of the bulk electrode underneath rGO layers for resistive connections of rGO layer[24-25] utilized in the conventional RGFET (**Figure 1b**) since the rGO layer is electrically coupled to the bulk electrode. That is, rGO and electrode complexes are regarded as a single combined resistor under the solution contact for a conventional RGFET, losing structural advantages offered by rGO layers at the solution interfaces. In addition, these rGO layers typically have imperfect coverage of rGO nanosheets on the electrode as shown in a scanning electron microscopy (SEM) image (**Figure 1a**), suggesting the inevitable of the uncovered electrode on interfacial potentials of the conventional RGFET system (**Figure 1b**) as being directly exposed to the solution.

An input impedance of commercial FET chip (CD4007) is at least 100 times higher than those of remote FG structure (**Figure S1**). This means that V_{th} of the RFGFET is an independent variable from factors that could alter the impedance of remote FG modules such as the thickness of the FG materials and SiO_2 and the contact area of media on the FG surface. It is noted that an equivalent circuit simplified with effective factors for RFGFET (**Figure 1a**) is identical to that of RGFET.[26]

Importantly, rGO RFGFET strongly resists drift and hysteresis in transfer curves measured for 50 gate voltage cycles in a pH7 media solution (**Figure 1d**). A high gate input impedance of the commercial FET and the SiO_2 dielectric of the FG module prevents the electrical current flow into the rGO, which leads to a large enhancement of stability by avoiding any undesirable factors impacting the rGO layers such as defects, interface traps, diffused ions, and redox reactions.

On the other hand, rGO layers processed identically to those in rGO RFGFET but used as a semiconducting channel for rGOFET (**Figure 1c**) reveal huge drifts and hysteresis in Dirac points (**Figure 1e**). rGOFET is a general structure used for biosensors where the rGO layer serves as both a semiconducting channel and a sensing layer. It is noted that such severe device instability (**Figure 1e**) was only caused by the electrical properties in the rGO semiconductor without any solution environments applied on rGO layers. This shows that charge transports for actual rGOFET biosensors are engaged by multiple indistinguishable factors such as mobility of rGO layers, defects, interface traps, diffused ions from solution to the rGO layer, redox reactions, and area of solution contact on the rGO layer. As a result, our RFGFET structure achieved a 50-fold decrease in the drift rate at the maximum compared to that of rGOFET (**Figure 1f**). The drift rate was calculated at a difference in the V_{th} levels of RGFET and Si-FET between the initial and saturated states divided by V_{th} at the initial; Dirac points of rGOFET were used for the calculation.

The V_{th} of RFGFET is comprised of the sum of independent components such as the V_{th} of a commercial FET (V_{FET}) and the electrochemical potentials associated with a solution/RG system.[27]

$$V_{th} = V_{FET} + E_{ref} + \phi_{lj} - \varphi_s + \chi_{sol} + \frac{\phi_{RG}}{q} \quad (1)$$

where E_{ref} is an absolute potential of the Ag/AgCl reference electrode (0.316 V, GAMRY Instruments), ϕ_{lj} is the liquid junction potential difference, φ_s is the surface potential at the electrolyte/sensing film interface, χ_{sol} is the electrolyte-insulator surface dipole potential, and ϕ_{RG} is the work function of the RG material. V_{FET} and the transconductance (G_m) of an innate FET (G_{FET}) remains stable at 1.55 V and 63 μS, respectively, over time without any drift and hysteresis before introducing a new variable of solution interface (**Figure S2**). Therefore, we further define a standard electrochemical potential of the remote FG material (E_{RG}) using equation (1).

$$E_{RG} = \phi_{lj} - \varphi_s + \chi_{sol} + \frac{\phi_{RG}}{q} \quad (2)$$

E_{RG} is a value only associated with the intrinsic electrochemical potentials of the FG surface, the media solution, and their interfaces resulting from their contacts, independent of the V_{FET} and E_{ref} which are varied by different experimental setups. Here, each E_{RG} and G_m of the RFGFET measured by a forward and reverse sweeping mode is referred to as E_{RG}^{For}, E_{RG}^{Rev}, G_m^{For}, and G_m^{Rev}, respectively. The hysteresis in E_{RG} (ΔE_{hys}) and in G_m (ΔG_{hys}) herein are calculated as the difference in

E_{RG} and G_m between forward and reverse sweeping mode at the saturation regime, respectively. G_m loss is calculated as $(G_{FET} - G_m)/G_{FET}$; a larger G_m loss will be shown at unstable solution interfaces and non-conductive surfaces.[28-29]

Mechanistic factors of rGO layers. Various thicknesses and coverages of rGO layers were prepared on a (3-aminopropyl)trimethoxysilane (APTMS)-treated SiO_2 surfaces by either controlling the concentrations of spin-coating GO solutions (**Figure S3a**) or using heat-assisted drop-casting methods (**Figure S3b**). Increasing the concentrations of spin-coating GO solutions (0.12, 0.24, 0.48 to 0.59 mg/ml) achieved denser GO networks, but still showed discontinuity over the remote FG surfaces (**Figure 2a, S3a**). In contrast, we obtained essentially continuous multilayer GO (**Figure 2b, S3b**) with ca. 4-nm-thickness (measured by atomic force microscopy (AFM) image in **Figure 1a)** using heat-assisted drop-casting methods with the high evaporation rate of GO solution under 120 °C (**Figure S4**). Additionally, ca. 2.5-μm-thick GO films were made on the edge of wafer for this heat-assisted drop-casting condition (**Figure S4**). It is noted that the lower plate temperature at 50 °C led to thick GO depositions over most of the wafer area (**Figure S4c**) instead of achieving multilayer GO.

Similar Raman spectra were observed for rGO layers made by different depositions of spin-coating and heat-assisted drop-casting, showing the D band at 1,350 cm^{-1}, which is attributed to the structural disorder, and the G band at 1,583 cm^{-1}, which is attributed to the bond stretching of sp^2 carbon atoms (**Figure 2c**). The appearance of weak and broad 2D (2,700 cm^{-1}) and D + G (2,940 cm^{-1}) bands in the GO spectrum is also a signature of edge disorder in graphitic sheets due to the incorporation of oxygen functional groups. Similar I_D/I_G ratios of 0.87, 0.95, and 0.91 were obtained for all rGO layers, which were spin-coated with 0.12 and 0.59 mg/ml GO solutions and made by heat-assisted drop-casting, respectively. Plenty of oxygen functional groups in all rGO layers were also found in an X-ray photoelectron spectroscopy (XPS) spectrum (**Figure 2d**), contributing to the pH-sensing capability of the rGO layers, as described in the next section.

pH sensitivity without GO layers on SiO_2 FG. The pH sensitivity of our starting materials such as a bare SiO_2 (**Figure 3a, S5**) and an APTMS-treated SiO_2 (**Figure 3b, S6**) was evaluated before introducing a GO layer. Initial negatively charged E_{RG}^{For} of both SiO_2 and APTMS/SiO_2 FG surface (gray-colored data in **Figure 3a, 3b**) drifted up to about 0 V of E_{RG}^{For}. No pH sensitivity was obtained for both surfaces (**Figure S7a**). Transfer curves measured in pH7 at the saturation regime (**Figure 3c)**, while remaining in mostly identical transfer curves during the forward-sweeping mode, show that the hydrophobicity of APTMS (**Figure S7b**)[22] promoted a slow response of water dipole orientations at the reverse sweeps and resultant large increase of E_{RG}^{Rev}.[29] The ΔE_{hys} of SiO_2 and APTMS/SiO_2 were measured to be 1.45 and 4.31 %, respectively.

This result corresponds to a higher G_m^{For} loss for APTMS (4.28%, **Figure 3b**) compared with that of the SiO_2 surface (2.53%, **Figure 3a**).

pH sensitivity with GO layers on FG. Even after the deposition of GO layers on APTMS/SiO_2, no pH responses appear without any reduction; each GO layer was spin-coated at a concentration of 0.12 mg/ml (**Figure 4a, S8**) and 0.59 mg/ml (**Figure 4b, S9**), respectively. All E_{RG}^{For} (**Figure 4a**, **4b)** was saturated near 0 V regardless of pH values, as were the cases of SiO_2 and APTMS/SiO_2. However, the presence of conductive GO layers under each condition was supported by higher G_m^{Rev} levels shown from spin-coated GO layers (62.4 μS for 0.12 mg/ml GO, 62.3 μS for 0.59 mg/ml GO) than APTMS (61.6 μS). On the other hand, 2.5 μm-thick GO films reveal insignificant ΔE_{dri}, ΔE_{hys}, ΔG_{hys}, and G_m loss, even though there is still no pH sensitivity (**Figure 4c, S10**). Lower levels of E_{RG}^{For} and E_{RG}^{Rev} of ca. -0.8 V describe highly positive-charged rGO surfaces while there are only 0.9% G_m loss with no ΔG_{hys}. There is a clear propensity that G_m^{For} increases with a higher conductivity of solution interface achieved by denser GO networks (**Figure S11**).

In summary, denser GO networks at the solution interface induce higher positive surface potentials with lower levels of E_{RG}^{For} and E_{RG}^{Rev} and ΔE_{hys}, as shown in a clear trend of transfer curves for each case measured for the pH7 buffer solution (**Figure 4d**). This reveals that highly conductive and hydrophilic GO films resist drift and hysteresis components. A very low concentration of GO networks at the solution-interface, such as 0.12 mg/ml GO has higher ΔE_{hys} of 192 mV and G_m^{For} loss of 4.75% than those of bare APTMS surfaces (ΔE_{hys}: 95 mV, G_m^{For} loss: 4.28%) as shown in **Figure 4f** and **4g**. For this type of analytical tools for interfacial analysis, higher G_m^{For} loss and ΔE_{hys} are mostly shown for the solution interface with increased hydrophobicity.[29] Based on our observation, we could hypothesize that hydrophobicity of solution interfaces with a very low concentration of rGO flakes on APTMS increased compared to that of a bare APTMS. It could be depicted that for lower GO concentrations most of the oxygen functional groups of monolayer GO on the surface are consumed in bonding with the amine groups on APTMS, which increases hydrophobicity. Furthermore, with increasing concentrations of GO, GO nanosheets begin to overlay on monolayer GO that had already bound to the surface via π–π interactions, which exposes oxygen functional groups to the solution-interface steadily and increases hydrophilicity (**inset of Figure 4f**), suggesting some threshold in the concentration of GO flakes at the solution-interface to achieve hydrophilic surfaces.

pH sensitivity with reduction of GO. We further investigated the effects of reduction temperatures on the pH sensitivity of the same GO films (**Figure 5)**. The pH responses of E_{RG}^{For} are shown for both 0.59 mg/ml GO (**Figure 5a, S12, S13, S14**) and 2.5 μm-thick GO films (**Figure 5b, S15, S16, S17**) reduced at 200, 300, and 400 °C, respectively. Overall E_{RG}^{For} levels of 0.59 mg/ml rGO steadily decreased at higher reduction temperatures (**Figure 5a**) due to the creation of positive charge carriers resulting from the reduction of diverse oxidized functional groups in GO sheets. Accordingly, increased conductivity resulting from higher reduction temperatures is shown as insignificant G_m loss (**Figure 5c, S18**), suggesting a trade-off between the conductivity and pH sensitivity of rGO. This is also supported by the decreasing propensity in the pH sensitivity of rGO layers with increasing reduction temperatures (**Figure 5d, S19**). In contrast, 2.5 μm-thick GO films increased E_{RG}^{For} levels overall with increasing reduction temperatures (**Figure 5b**), which is an opposite trend to that of 0.59 mg/ml GO. Without reductions, 2.5 μm-thick GO films already have plenty of positive charges because of the denser GO networks as shown in the lower E_{RG}^{For} levels at ca. -0.8V (**Figure 4c**). Thus, the E_{RG}^{For} levels for 2.5 μm-thick GO films are more affected by the losing effects of pH sensitivity from reductions.

Our results so far suggest that hydrophilic GO surfaces that include oxygen functional groups are more sensitive to changes in surface potentials, and that the high conductivity of GO surfaces stabilizes solution interfaces, thereby reducing hysteresis and drift components. Unfortunately, the higher conductivity achieved by higher reduction temperatures increases the hydrophobicity of the rGO surface. Thus, we sought to find the optimal pH sensitivity of rGO by increasing conductivity in terms of denser rGO networks under a minimized reduction temperature at 200 °C. Similar pH sensing properties were observed as rGO began to construct rGO networks that are dense enough over FG surfaces (i.e., 0.48 mg/ml rGO, 0.59 mg/ml rGO, multilayer GO made by drop-casting, **Figure 5e, 5f**). CV values for each pH from multilayer rGO are < 3% over all pH ranges; each CV value was calculated by using raw values of V_{th} for each pH over 9 samples of rGO. Finally, the multilayer rGO made by the heat-assisted drop-casting method shows the lowest drift rate of 2%, thereby maintaining a high pH sensitivity of 54 mV/pH with an R^2 value of 0.998 (**Figure 5f**). More importantly, the optimal rGO layer revealed a 90% yield (9 samples out of total 10) in showing the pH sensitivity (54 mV/pH) due to enhanced stability and reproducibility of electrochemical properties of the RFGFET structure.

Spike protein detection using rGO RFGFET. Quantification of S protein concentrations is done by using optimized multilayer GO layers above. We tracked a shifting propensity of transfer curves of rGO RFGFET depending on the surface modification for S protein detection (**Figure 6a**). Summarized V_{th} and G_{m} loss for each interfacial condition is

shown in **Figure 6b**. The V_{th} of bare SiO_2 and APTMS/SiO_2 surfaces are close to 1.86 V in 0.05× PBS. On the other hand, the presence of multilayer rGO on an APTMS/SiO_2 surface turns over the electric properties of interfaces by inducing strongly positive charges on the FG surface (i.e., V_{th} of rGO: 1.35 V) due to a large number of hole carriers inside the rGO layers. The increase in G_m^{For} (G_m^{For} of APTMS: 60.3 μS → G_m^{For} of rGO: 62.7 μS) also suggests the formation of highly conductive rGO layers at the solution-FG interface.

In **Figure 6b**, neutralizing antibodies and the BSA blocking layer, however, increase V_{th} relative to bare rGO surfaces (V_{th} of antibody/BSA: 1.43 V). It is noted that insignificant device-to-device variations are shown for all V_{th} levels with antibody probes on the rGO, which were obtained by averaging the absolute values of each V_{th} over at least eight samples. V_{th} levels of antibody-functionalized rGO layers rather have a dependency of BSA incubation time. That is, overnight BSA incubation largely increases V_{th} close to those of bare SiO_2 and APTMS/SiO_2 while increasing G_m^{For} loss of the system. This suggested a formation of thick layer of protein in terms of hydrophobic bonding of protein on rGO surfaces covering the most 2D rGO layer areas for this long-term incubation. The resultant non-conductive protein interfaces led to high V_{th} levels close to 1.8 V which were shown by non-conductive surfaces such as SiO_2 or APTMS/SiO_2 surfaces. It is noted that this characterization could only be done by achieving the isolation of 2D materials of rGO layer in the solution interface by our RFGFET structure.

We measured eight different rGO devices with 4 hours incubation with BSA and n-antibodies (250 μg/ml) in the following S protein tests. Increasing concentrations of S proteins on an antibody-functionalized rGO surface induced additional positive surface potentials[5], with saturation occurring at the concentration of S proteins above 34 ng/ml (**Figure 6c, S20**). ΔV_{th} calculated at a difference in V_{th} at each S protein concentration and baseline V_{th} is used to minimize effects of baseline V_{th} changed by BSA incubations on the calculation of sensitivity. Each ΔV_{th} point in Figure 6c was obtained from the last point of ΔV_{th} for 20 measurements (5 min testing time) at each concentration in **Figure S21**. All ΔV_{th} sensing curves obtained after measurements for at least 2.5 min displayed stable sensing curves in ΔV_{th} but longer measurement time of 5 min was chosen to obtain stable ΔV_{th} levels in quasi-equilibrium, which minimizes the impact of measurement time and drift on the sensitivity of devices (**Figure S22**).

The increased concentration of neutralizing antibodies on the rGO surface from 20 to 250 μg/ml revealed a higher sensitivity and resolution over all ranges of S protein concentrations. For rGO layers functionalized with 250 μg/ml of neutralizing antibody, the sensitivity was measured to be 6.3 mV/dec, with an R^2 of 0.986 at a concentration range of 3.4

pg/ml to 34 ng/ml in a PBS buffer solution. We defined a LOD at the concentration of S proteins showing a clear signal in ΔV_{th} which is distinguishable from the maximum fluctuation in baselines (ca. 10 mV) that could occur for any measurement conditions (**Figure S22)**. Thus, the guaranteed LOD is a few pg/ml. After measuring the S protein, the FG surfaces were washed five times with a pure PBS solution and then sequentially measured in a pure PBS again to confirm the remaining binding signals after washing (**Figure S21**). A higher sensitivity was maintained for rGO surfaces functionalized with 250 μg/ml antibodies, possibly because of a larger number of binding events between the antibody and the S protein, even after washing. After completing all the measurements, we then measured the FG surface for the pH2 buffer solution (**Figure S21**). A sharp shift in the V_{th} in pH2 resulted from $\Delta\varphi_s$ of the rGO layers by pH, indicating the presence of sturdy rGO layers, even after conducting all the sensing experiments.

Opposite ΔV_{th} was observed from a bare rGO layer contacted with the same concentrations of S protein and BSA (**Figure 6d, S23**), supporting the specificity of our results above and strong non-specific binding of proteins on rGO surfaces in terms of hydrophobic interactions. This result, however, suggests the essential needs for blocking layers for FET bioelectronics to prevent further non-specific binding. Our electrical detection signals were verified by the ELISA experiments shown in **Figure 6e**. We used antibody conjugated-rGO substrates processed identically to Figure 6c as a starting surface for ELISA testing by directly placing them on a new well plate to process the rest of ELISA protocol. The antibody conjugated-rGO surface with S proteins showed distinguishable signals compared with those with bare rGO surfaces without antibody conjugation as the control group. This result explicitly showed n-antibodies were successfully functionalized on our rGO surfaces. Moreover, the ELISA signals further increased by 50% by increasing the antibody concentration from 20 μg/mL to 250 μg/mL (**Figure 6e**), which corresponds to our electrical measurements.

Finally, the detection of S proteins was performed in a solution mixture of artificial saliva and 0.05× PBS with a ratio of 1:20 in order to demonstrate the potential of our device platform for practical diagnosis (**Figure 6f**). Each ΔV_{th} in **Figure 6f** is an average of 5 samples. The PBS solution in this mixture plays a role of controlling pH of testing media at pH7.4. This dilution ratio was chosen by finding the minimum dilution ratio of the PBS solution that preserves the pH value of a mixture solution at 7.4 (**Figure S24**). This is especially important for reproducibility of signals because divergent pH of patient's saliva in a range from 6.2 to 7.6 could affect changes in isoelectric point of proteins on sensing surfaces. The sensitivity in saliva-relevant fluids was measured to be 5.1 mV/dec, with an R^2 of 0.984 and CV < 3% (from raw values of V_{th} over 5 samples), in a range from 500 fg/ml to 5 ug/ml (**Figure 6f**) while the guaranteed LOD is at pg/ml considering

the maximum fluctuation value (ca. 10 mV) in baseline. Our LOD is not as low as other pervious solution-gated 2D FET sensor research[6] although both the RFGFET and conventional solution-gated structures have the same solution interface, i.e., between the 2D material and the media solution. For RFGFET, changes in surface potentials are capacitively transferred to the FET transducer as the 2D interface is isolated by the insulator, which suppresses many noise factors but also leads to some loss in specific signals due to the additional process for signal transmission over the insulator. In contrast, for conventional solution-gated structures, all changes in surface potentials on the 2D interface are directly read out by the same 2D semiconductor, which enables higher sensitivity and lower LOD for targeting biomarkers than our RFGFET but allows non-ideal signaling to be incorporated into output signals. We would like to emphasize again that the success of COVID-19 FET sensors now depends on how reliable and stable devices are rather than how sensitive they are because reported FET sensors display a sensitivity that is more than enough compared to conventional optical-based analytical tools.[9]

Conclusion

To elucidate the critical mechanistic factors behind the instability of rGO layers, we constructed an rGO sensing membrane in the RFGFET setup for rapid and reliable diagnostic tools for detecting COVID-19 as an alternative to current LFAs and RT-PCR methods. We performed a comprehensive systematic analysis of the pH sensing properties of rGO layers affected by their thickness, coverage, and reduction temperature. FG configuration is essential for reducing large device-to-device variations of 2D materials-based bioelectronics. The high conductivity of rGO obtained by high reduction temperatures increased hydrophobicity by reducing oxygen functional groups. A high conductivity achieved by dense networks of rGO plus a minimum reduction temperature leads to the optimal transducing properties, showing a pH sensitivity of 54 mV/pH with an R^2 value of 0.998 and CV < 3%, 90% yield, and a low drift ratio of 2%. As a proof-of-concept, we demonstrated highly reproducible and reliable detection of the COVID-19 S proteins in both 0.05× PBS and a saliva mixture. In response to concentrations of S proteins, our RFGFET sensors displayed the sensitivity of 6.3 mV/dec (3.4 pg/ml to 34 ng/ml) for a 0.05× PBS environment and 5.1 mV/dec (500 fg/ml to 5 μg/ml) with CV < 3% for a saliva mixture solution. The guaranteed LOD of S proteins was at a few pg/ml. The sensitivity and specificity of the SARS-CoV-2 S protein were also confirmed by ELISA. This platform may have an immense effect on positioning FET bioelectronics in a clinical setting for COVID-19 detection.

Experimental Section

RG module fabrication. The cleaned 4-in silicon wafer with a 300-nm-thick SiO_2 was treated with an oxygen plasma for 5 min at 250 W under an O_2 flow rate of 10 sccm in order to introduce hydroxyl groups on SiO_2 surfaces. The wafer was fully immersed and incubated in a 5% APTMS (Sigma Aldrich, 281778) solution dissolved in ethanol (Sigma Aldrich, 459836) for 1 h. After washing the surface, the wafer was heated at 120 °C for 20 min. Then, GO solutions of 0.12, 0.24, 0.48, and 0.59 mg/ml were prepared by dispersing GO (ACS Material, 7782-42-5) in deionized water aided by ultrasonication for 20 min. Each GO solution was spin-coated on an APTMS/SiO_2 wafer under 1,600 RPM for 1 min. In heat-assisted drop-casting, 16 ml of 0.12 mg/ml solution was drop-casted over the entire area of a 4-in wafer and then baked at 120 °C for 1 h. The GO/APTMS/SiO_2 wafers were sliced to 1 x 2 cm^2 for an RG module. The post-annealing of each GO RG module was performed using a horizontal furnace for 5 min under an argon gas environment, with temperatures of 200, 300, and 400 °C. The surface images were acquired by scanning electron microscopy (SEM).

Preparation of n-antibody-conjugated rGO layers and testing media. The fabricated rGO RG modules were fully immersed in a 10 mg/ml 1-pyrenebutyric acid N-hydroxysuccinimide ester, 95% (PBASE) (Santa Cruz Biotechnology, 114932-60-4) solution for 2 h. After washing the rGO surfaces, 20 or 250 μg/ml SARS-CoV-2 neutralizing antibody (Sino Biological, 40592-MM57) was incubated on the rGO surface at least for 4 h. Sequentially, 10 mg/ml BSA solution dissolved in 1× PBS was added at least for 4 h. The SARS-CoV-2 S protein (Sino Biological, 40592-V08B) was diluted in 0.05× PBS to concentrations of 34 fg/ml to 3.4 μg/ml for testing media. Also, S proteins were diluted in a mixture solution of 0.05× PBS and artificial saliva (Fisher Scientific, NC1873811) with a ratio of 20:1 to concentrations of 500 fg/ml to 5 μg/ml for testing media. Initial pH of the artificial saliva was 6.

Electrical measurement system. A commercial FET (CD4007UB) was used as a transducer to investigate the fabricated RGs, as previously discussed. An aqueous solution at a defined pH was placed on each RG surface. An Ag/AgCl reference electrode was placed in the solution in order to apply the gate bias for all measurements. All transfer curves were measured using a Keithley 4200A semiconductor analyzer with a drain voltage set at 50 mV, and the gate voltage remained in the double-sweep mode. Transfer curves of the RGFET were repeatedly measured for 20 cycles under a pH solution in a range from pH2 to 11. The V_{th} was calculated as the gate voltage corresponding to drain current of 1 μA in each transfer curve. The G_m of each RGFET was calculated at its maximum value.

ELISA protocol. The antibody-conjugated rGO substrates sliced to 0.5 x 0.5 cm^2 were placed in a new 48-well plate. Each rGO substrate was washed gently three times with 1× PBS including 0.05% Tween 20. Sequentially, 200 μL biotinylated spike protein prepared in 1× assay buffer at a concentration of 1 μg/ml (Biolegend) was incubated on each rGO substrate for 2 h under 300 rpm at room temperature. After gently washing each rGO surface three to five times with 1× PBS including 0.05% Tween 20, 200 μl avidin-HRP (Biolegend) diluted 1,000 times in 1× assay buffer was incubated for 30 min with 300 rpm shaking under room temperature, then gently washed five times using 1× PBS including 0.05% Tween 20. The samples were soaked in the buffer for 30 s during each wash. Then, 200 mL 3,3′,5,5′-tetramethylbenzidine substrate was further added into each well and incubated for 30 min under dark. Finally, 200 μL stop reagent (2N H_2SO_4) was added, and the resulting solutions in each well were transferred to another new 48-well plate for measurements. The absorbance values were read at 450 nm using a microplate reader.

Author Contributions

Electrical Measurement, sample Fabrication, interpretation of data were carried out by H.-J. Jang, X. Sui, W. Zhuang, Y. Wang, and B. Ryu. ELISA measurement and analysis were performed by X. Huang and M. Chen, J. Huang. The manuscript was prepared by H.-J. Jang, H. Pu, and N. Ankenbruck, and J. Chen. All authors examined and commented on the manuscript. The project was guided by J. Chen., K. Beavis, and J. Huang.

Supporting Information

Electrical properties of Si-FET transducer. pH responses of transfer curves of RGFET with RGs of SiO_2, APTMS/SiO_2, and rGO/APTMS/SiO_2 which is reduced at different reduction temperatures and coverages. E_{RG}^{For} distributions of bare rGO and antibody-functionalized rGO layers for increasing spike proteins. SEM images of rGO layers made by heat-assisted drop-casting method.

Declaration of competing interest

The authors declare no competing financial interest.

Acknowledgements

This work was supported by a Walder Foundation grant and a University of Chicago Big Ideas Generator grant.

Figure captions

Figure 1. (a) Schematic images and equivalent circuits of the RFGFET system. AFM and SEM images of the 2D rGO layer on the FG surface made by a heat-assisted drop-casting method and reduced at 200 °C. Schematic images of (b) conventional RGFET and (c) rGOFET structure. (d) Transfer curves of rGO RFGFET measured for 50 gate voltage cycles in pH7 solution. (e) Transfer characteristics of rGOFET with rGO identically processed to (a) measured for 50 gate voltage cycles via the bottom gate without any solution environment on the rGO layer. (f) Drift rate of Si-FET, rGO RFGFET, and rGOFET.

Figure 2. SEM images of GO layers (a) spin-coated with 0.12 and 0.59 mg/ml GO solutions and (b) made by a heat-assisted drop-casting method. (c) Raman and (d) XPS spectra of rGO layers spin-coated with 0.12 and 0.59 mg/ml GO solutions, and multilayer rGO made by a heat-assistant drop-casting method, respectively. All rGO layers were reduced at 200 °C.

Figure 3. E_{RG} and G_m distributions of (a) SiO_2 and (b) APTMS/SiO_2 that are measured by forward- and reverse-sweeping modes with increasing pH values over time. Each E_{RG} and G_m is averaged with at least seven trials for each measurement. (c) Representative transfer curves of SiO_2 and APTMS/SiO_2 at saturation regime in pH7.

Figure 4. E_{RG} and G_m distributions over at least four samples with pristine GO surfaces spin-coated with (a) 0.12 mg/ml and (b) 0.59 mg/ml GO solutions and (c) 2.5 μm-thick GO films for increasing pH over time. (d) Representative transfer curves of spin-coated and drop-casted GO layers in pH7 at saturation regime. (e) E_{RG}^{For} distributions of spin-coated and drop-casted GO layers vs. pH value. (f) G_m loss in pH7 vs. the type of RG surface. Inset shows schematics for surface property changes by concentrations of GO flakes. (g) E_{RG} distributions in pH7 at saturation regime vs. the type of RG surface.

Figure 5. E_{RG}^{For} distributions of (a) 0.59 mg/ml GO layers and (b) 2.5 μm-thick GO films at different reduction temperatures over at least four samples as a function of increasing pH over time. (c) pH sensitivity of 0.12 and 0.59 mg/ml GO layers and 2.5 μm-thick GO film as a function of reduction temperature. pH sensitivity is directly calculated by using E_{RG}^{For} values. (d) G_m reduction of 0.12 and 0.59 mg/ml GO layers and 2.5 μm-thick GO film in pH7 vs. the reduction temperature. (e) E_{RG}^{For} distributions of spin-coated or drop-casted rGO films over at least four samples as a function of increasing pH; CV values of multilayer rGO were calculated by using V_{th} of 9 different multilayer rGO layers for each pH showing a 90% yield (9 samples out of total 10). (f) pH sensitivity and drift rates in pH7 solutions.

Figure 6. (a) Response of transfer curves depending on surface modifications on FG. (b) V_{th} and G_m^{For} distributions depending on surface modification on FG. (c) ΔV_{th} of antibody-functionalized rGO (20 or 250 μg/ml antibody) vs.

concentrations of S protein. (d) ΔV_{th} or G_m^{For} loss of bare rGO vs. concentrations of S protein or BSA. (e) ELISA detection of S protein using an antibody-conjugated rGO surface. (f) ΔV_{th} and CV of antibody-functionalized rGO (250 μg/ml antibody) over 5 different devices vs. concentrations of S protein in an artificial saliva mixture.

References

1. Yuki, K.; Fujiogi, M.; Koutsogiannaki, S., COVID-19 Pathophysiology: A Review. Clin. Immunol. **2020**, 215, 108427.
2. Peck, K. R., Early Diagnosis and Rapid Isolation: Response to COVID-19 Outbreak in Korea. Clin. Microbiol. Infec. **2020**, 26, 805-807.
3. Afzal, A., Molecular Diagnostic Technologies for COVID-19: Limitations and Challenges. J. Adv. Res. **2020**, 26, 149-159.
4. Perchetti, G. A.; Huang, M. L.; Mills, M. G.; Jerome, K. R.; Greninger, A. L., Analytical Sensitivity of the Abbott BinaxNOW COVID-19 Ag Card. J. Clin. Microbiol. **2021**, 59, e02880-20.
5. Zamzami, M. A.; Rabbani, G.; Ahmad, A.; Basalah, A. A.; Al-Sabban, W. H.; Ahn, S. N. Choudhry, H., Carbon Nanotube Field-Effect Transistor (CNT-FET)-based Biosensor for Rapid Detection of SARS-CoV-2 (COVID-19) Surface Spike Protein S1. Bioelectrochemistry **2021**, 143, 107982.
6. Seo, G.; Lee, G.; Kim, M. J.; Baek, S. H.; Choi, M.; Ku, K. B.; Lee, C. S.; Jun, S.; Park, D.; Kim, H. G.; Kim, S. J.; Lee, J. O.; Kim, B. T.; Park, E. C.; Kim, S. I. Rapid Detection of COVID-19 Causative Virus (SARS-CoV-2) in Human Nasopharyngeal Swab Specimens Using Field-Effect Transistor-Based Biosensor (vol 14, pg 5135, 2020). Acs Nano **2020**, 14, 12257-12258.
7. Li, J.; Wu, D.; Yu, Y.; Li, T.; Li, K.; Xiao, M. M.; Li, Y.; Zhang, Z. Y.; Zhang, G. J. Rapid and Unamplified Identification of COVID-19 with Morpholino-modified Graphene Field-Effect Transistor Nanosensor. Biosens. Bioelectron. **2021**, 183, 113206.
8. Fathi-Hafshejani, P.; Azam, N.; Wang, L.; Kuroda, M. A.; Hamilton, M. C.; Hasim, S.; Mahjouri-Samani, M. Two-Dimensional-Material-Based Field-Effect Transistor Biosensor for Detecting COVID-19 Virus (SARS-CoV-2). ACS Nano **2021**, 15, 11461–11469.
9. Baker, A.; Richards, S. J.; Congdon, T.; Hasan, M.; Guy, C.; Zwetsloot, A.; Gallo, A.; Lewandowski, J.; Stansfeld, P.; Straube, A.; Walker, M.; Chessa, S.; Pergolizzi, G.; Dedola, S.; Field, R.; Gibson, M., The SARS-COV-2 Spike Protein Binds Sialic Acids, and Enables Rapid Detection in a Lateral Flow Point of Care Diagnostic Device. *ACS Central. Sci.* **2021,** *7* (2), 379-380.
10. Kutovyi, Y.; Hlukhova, H.; Boichuk, N.; Menger, M.; Offenhausser, A.; Vitusevich, S. Amyloid-beta Peptide Detection via Aptamer-Functionalized Nanowire Sensors Exploiting Single-Trap Phenomena. Biosens. Bioelectron. **2020**, 154, 112053.
11. Alabsi, S. S.; Ahmed, A. Y.; Dennis, J. O.; Khir, M. H. M.; Algamili, A. S. A Review of Carbon Nanotubes Field Effect-Based Biosensors. IEEE Access **2020**, 8, 69509-69521.
12. Sarkar, D.; Liu, W.; Xie, X. J.; Anselmo, A. C.; Mitragotri, S.; Banerjee, K. MoS2 Field-Effect Transistor for Next-Generation Label-Free Biosensors. ACS Nano **2014**, 8, 3992-4003.
13. Tsang, D. K. H.; Lieberthal, T. J.; Watts, C.; Dunlop, I. E.; Ramadan, S.; Hernandez, A. E. D.; Klein, N., Chemically Functionalised Graphene FET Biosensor for the Label-free Sensing of Exosomes. Sci. Rep. **2019**, 9, 13946.
14. Hwang, M. T.; Heiranian, M.; Kim, Y.; You, S.; Leem, J.; Taqieddin, A.; Faramarzi, V.; Jing, Y. H.; Park, I.; van der Zande, A. M.; Nam, S.; Aluru, N. R.; Bashir, R., Ultrasensitive Detection of Nucleic Ccids Using Deformed Graphene Channel Field Effect Biosensors. Nat. Commun. **2020**, 11, 1543.
15. Park, D.; Kim, J. H.; Kim, H. J.; Lee, D.; Lee, D. S.; Yoon, D. S.; Hwang, K. S., Multiplexed Femtomolar Detection of Alzheimer's Disease Biomarkers in Biofluids Using a Reduced Graphene Oxide Field-Effect Transistor. Biosens. Bioelectron. **2020**, 167, 112505.
16. Fan, Q.; Wang, L. D.; Xu, D.; Duo, Y. H.; Gao, J.; Zhang, L.; Wang, X. B.; Chen, X.; Li, J. H.; Zhang, H., Solution-Gated Transistors of Two-Dimensional Materials for Chemical and Biological Sensors: Status and Challenges. Nanoscale **2020**, 12 (21), 11364-11394.
17. Fu, W. Y.; Nef, C.; Knopfrnacher, O.; Tarasov, A.; Weiss, M.; Calame, M.; Schonenberger, C., Graphene Transistors Are Insensitive to pH Changes in Solution. Nano Lett. **2011**, 11, 3597-3600.
18. Ang, P. K.; Chen, W.; Wee, A. T. S.; Loh, K. P., Solution-Gated Epitaxial Graphene as pH Sensor. J. Am. Chem. Soc. **2008**, 130, 14392-14393.
19. Yu, Q. K.; Lian, J.; Siriponglert, S.; Li, H.; Chen, Y. P.; Pei, S. S., Graphene Segregated on Ni surfaces and Transferred to Insulators. Appl. Phys. Lett. **2008**, 93, 113103.
20. Kim, K. S.; Zhao, Y.; Jang, H.; Lee, S. Y.; Kim, J. M.; Kim, K. S.; Ahn, J. H.; Kim, P.; Choi, J. Y.; Hong, B. H., Large-scale Pattern Growth of Graphene Films for Stretchable Transparent Electrodes. Nature **2009**, 457, 706-710.
21. Yan, F.; Zhang, M.; Li, J. H. Solution-Gated Graphene Transistors for Chemical and Biological Sensors. Adv. Healthc. Mater. **2014**, 3, 313-331.

22. Howarter, J. A.; Youngblood, J. P., Surface Modification of Polymers with 3-aminopropyltriethoxysilane as a General Pretreatment for Controlled Wettability. Macromolecules **2007**, 40, 1128-1132.
23. Ke, Z. L.; Oton, J. Q.; Qu, K.; Cortese, M.; Zila, V.; McKeane, L.; Nakane, T.; Zivanov, J.; Neufeldt, C. J.; Cerikan, B.; Lu, J. M.; Peukes, J.; Xiong, X. L.; Krausslich, H. G.; Scheres, S. H. W.; Bartenschlager, R.; Briggs, J. A. G., Structures and Distributions of SARS-CoV-2 Spike Proteins on Intact Virions. Nature **2020**, 588, 498-502.
24. Li, Y. R.; Chang, S. H.; Chang, C. T.; Tsai, W. L.; Chiu, Y. K.; Yang, P. Y.; Cheng, H. C. High-sensitivity Extended-Gate Field-Effect Transistors as pH sensors with Oxygen-Modified Reduced Graphene Oxide Films Coated on Different Reverse-Pyramid Silicon Structures as Sensing Heads. Jpn. J. Appl. Phys. **2016**, 55, 04em08
25. Li, L.; Ma, X. F.; Xiao, Y.; Wang, Y. Construction and Application of Graphene Oxide-Bovine Serum Albumin Modified Extended Gate Field Effect Transistor Chiral Sensor. Sensors **2021**, 21, 3921.
26. Jang, H. J.; Wagner, J.; Li, H.; Zhang, Q. Y.; Mukhopadhyaya, T.; Katz, H. E., Analytical Platform To Characterize Dopant Solution Concentrations, Charge Carrier Densities in Films and Interfaces, and Physical Diffusion in Polymers Utilizing Remote Field-Effect Transistors. *J. Am. Chem. Soc.* **2019,** *141*, 4861-4869.
27. Pullano, S. A.; Critello, C. D.; Mahbub, I.; Tasneem, N. T.; Shamsir, S.; Islam, S. K.; Greco, M.; Fiorillo, A. S., EGFET-Based Sensors for Bioanalytical Applications: A Review. Sensors **2018**, 18, 4042.
28. Jang, H. J.; Song, Y. J.; Wagner, J.; Katz, H. E., Suppression of Ionic Doping by Molecular Dopants in Conjugated Polymers for Improving Specificity and Sensitivity in Biosensing Applications. ACS Appl. Mater. Inter. **2020**, 12, 45036-45044
29. Jang, H. J.; Wagner, J.; Song, Y. J.; Lee, T.; Katz, H. E., Carboxylic Acid-Functionalized Conjugated Polymer Promoting Diminished Electronic Drift and Amplified Proton Sensitivity of Remote Gates Compared to Nonpolar Surfaces in Aqueous Media. Adv. Electron. Mater. **2020**, 6, 1901073.

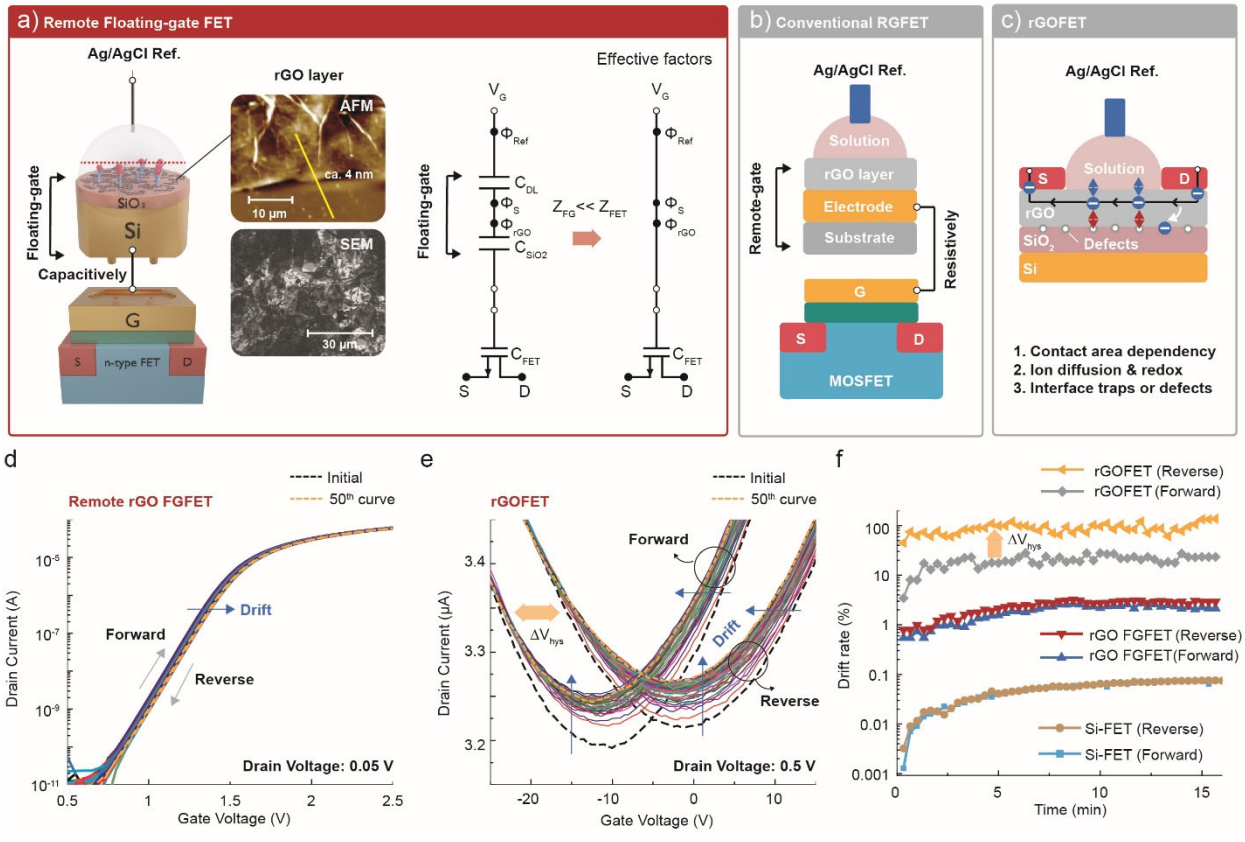
a) Remote Floating-gate FET
Ag/AgCl Ref.
rGO layer
AFM
ca. 4 nm
10 μm
SEM
30 μm
Floating-gate
Capacitively
SiO2
Si
G
S
n-type FET
D
Effective factors
Floating-gate
Z_FG << Z_FET
S
D
b) Conventional RGFET
Ag/AgCl Ref.
Solution
rGO layer
Electrode
Substrate
Remote-gate
Resistively
G
S
D
MOSFET
c) rGOFET
Ag/AgCl Ref.
Solution
S
D
rGO
SiO2
Defects
Si
1. Contact area dependency
2. Ion diffusion & redox
3. Interface traps or defects
d
Remote rGO FGFET
Initial
50th curve
Forward
Drift
Reverse
Drain Voltage: 0.05 V
Drain Current (A)
Gate Voltage (V)
e
rGOFET
Initial
50th curve
Forward
Drift
Reverse
ΔV_hys
Drain Voltage: 0.5 V
Drain Current (μA)
Gate Voltage (V)
f
rGOFET (Reverse)
rGOFET (Forward)
ΔV_hys
rGO FGFET (Reverse)
rGO FGFET(Forward)
Si-FET (Reverse)
Si-FET (Forward)
Drift rate (%)
Time (min)

Figure 1

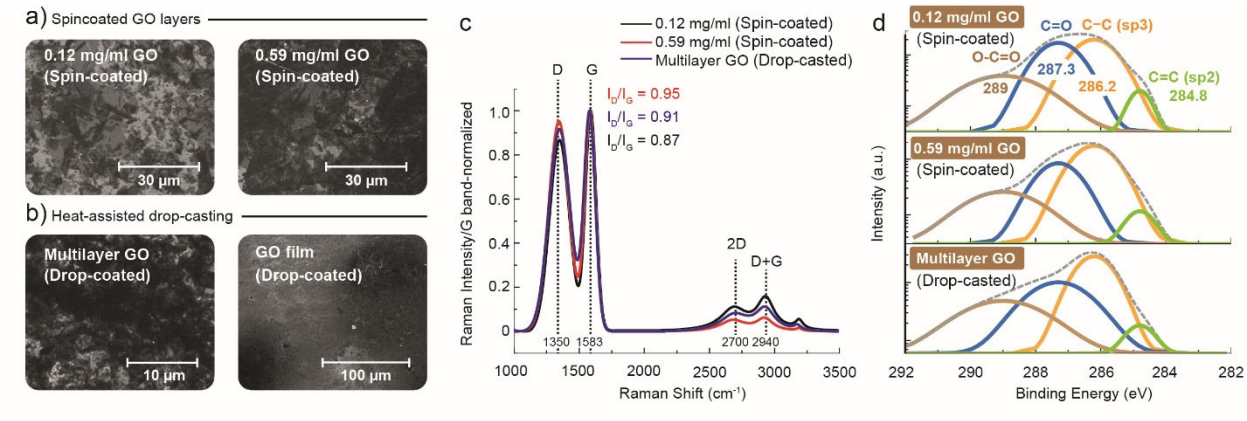
a) Spincoated GO layers
0.12 mg/ml GO (Spin-coated)
30 μm
0.59 mg/ml GO (Spin-coated)
30 μm
b) Heat-assisted drop-casting
Multilayer GO (Drop-coated)
10 μm
GO film (Drop-coated)
100 μm
c
0.12 mg/ml (Spin-coated)
0.59 mg/ml (Spin-coated)
Multilayer GO (Drop-casted)
D
G
2D
D+G
I_D/I_G = 0.95
I_D/I_G = 0.91
I_D/I_G = 0.87
1350 1583
2700 2940
Raman Intensity/G band-normalized
Raman Shift (cm^{-1})
d
0.12 mg/ml GO (Spin-coated)
C=O
C−C (sp3)
O-C=O
289
287.3
286.2
C=C (sp2)
284.8
0.59 mg/ml GO (Spin-coated)
Multilayer GO (Drop-casted)
Intensity (a.u.)
Binding Energy (eV)

Figure 2

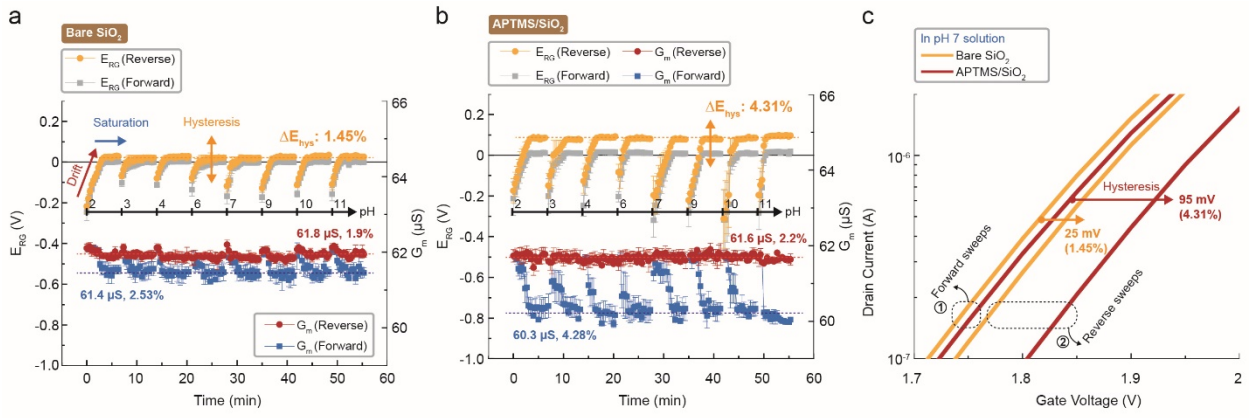
a
Bare SiO2
ERG (Reverse)
ERG (Forward)
Saturation
Hysteresis
ΔEhys: 1.45%
Drift
pH
61.8 μS, 1.9%
61.4 μS, 2.53%
Gm (Reverse)
Gm (Forward)
ERG (V)
Gm (μS)
Time (min)
b
APTMS/SiO2
ERG (Reverse)
Gm (Reverse)
ERG (Forward)
Gm (Forward)
ΔEhys: 4.31%
pH
61.6 μS, 2.2%
60.3 μS, 4.28%
ERG (V)
Gm (μS)
Time (min)
c
In pH 7 solution
Bare SiO2
APTMS/SiO2
Hysteresis
95 mV
(4.31%)
25 mV
(1.45%)
Forward sweeps
Reverse sweeps
Drain Current (A)
Gate Voltage (V)

Figure 3

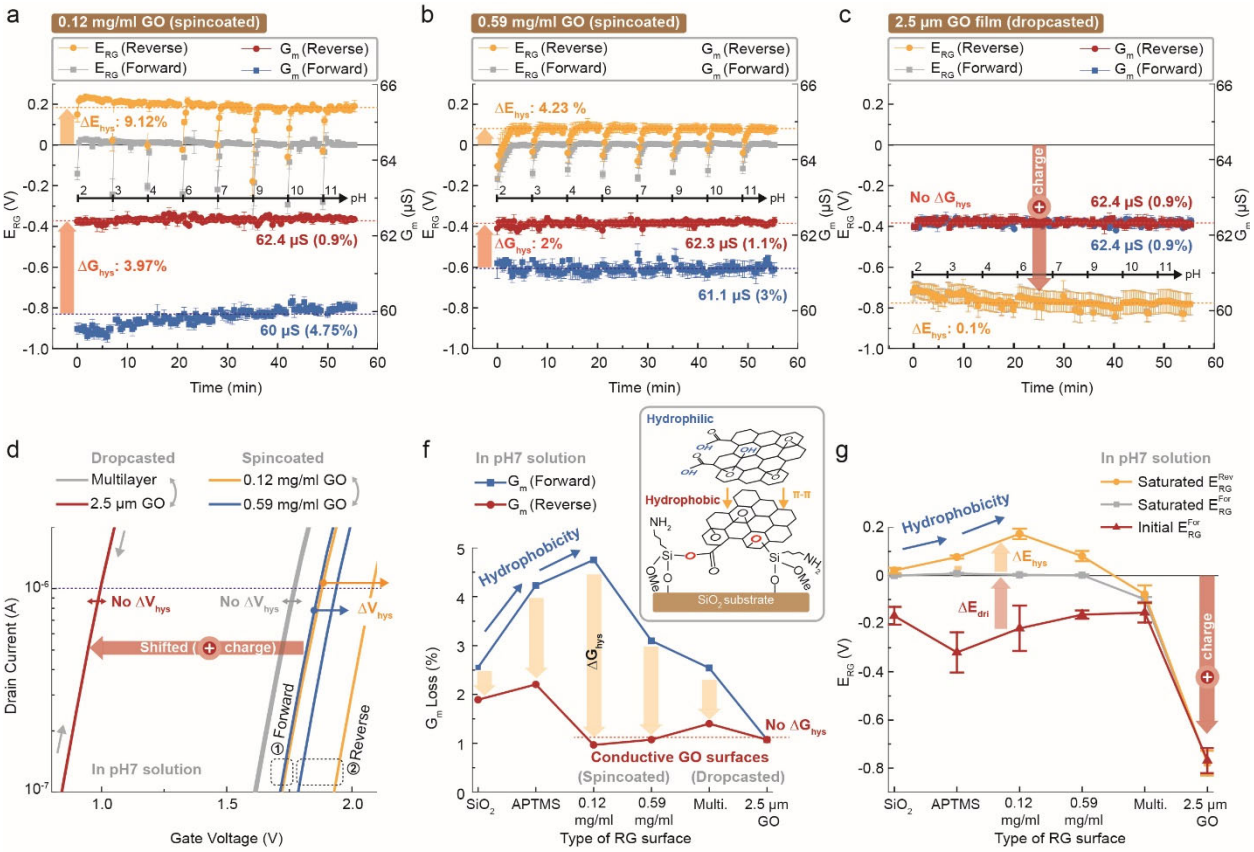
a
0.12 mg/ml GO (spincoated)
b
0.59 mg/ml GO (spincoated)
c
2.5 μm GO film (dropcasted)
Time (min)
pH
No ΔG_hys
charge
62.4 μS (0.9%)
62.3 μS (1.1%)
61.1 μS (3%)
60 μS (4.75%)
ΔE_hys: 9.12%
ΔE_hys: 4.23 %
ΔE_hys: 0.1%
ΔG_hys: 3.97%
ΔG_hys: 2%
d
Dropcasted
Spincoated
Multilayer
2.5 μm GO
0.12 mg/ml GO
0.59 mg/ml GO
No ΔV_hys
ΔV_hys
Shifted (+ charge)
Forward
Reverse
In pH7 solution
Drain Current (A)
Gate Voltage (V)
f
In pH7 solution
Hydrophilic
Hydrophobic
π-π
SiO2 substrate
Hydrophobicity
ΔG_hys
No ΔG_hys
Conductive GO surfaces
(Spincoated)
(Dropcasted)
G_m Loss (%)
SiO2
APTMS
0.12 mg/ml
0.59 mg/ml
Multi.
2.5 μm GO
Type of RG surface
g
In pH7 solution
Saturated E_RG^Rev
Saturated E_RG^For
Initial E_RG^For
Hydrophobicity
ΔE_hys
ΔE_dri
charge

Figure 4

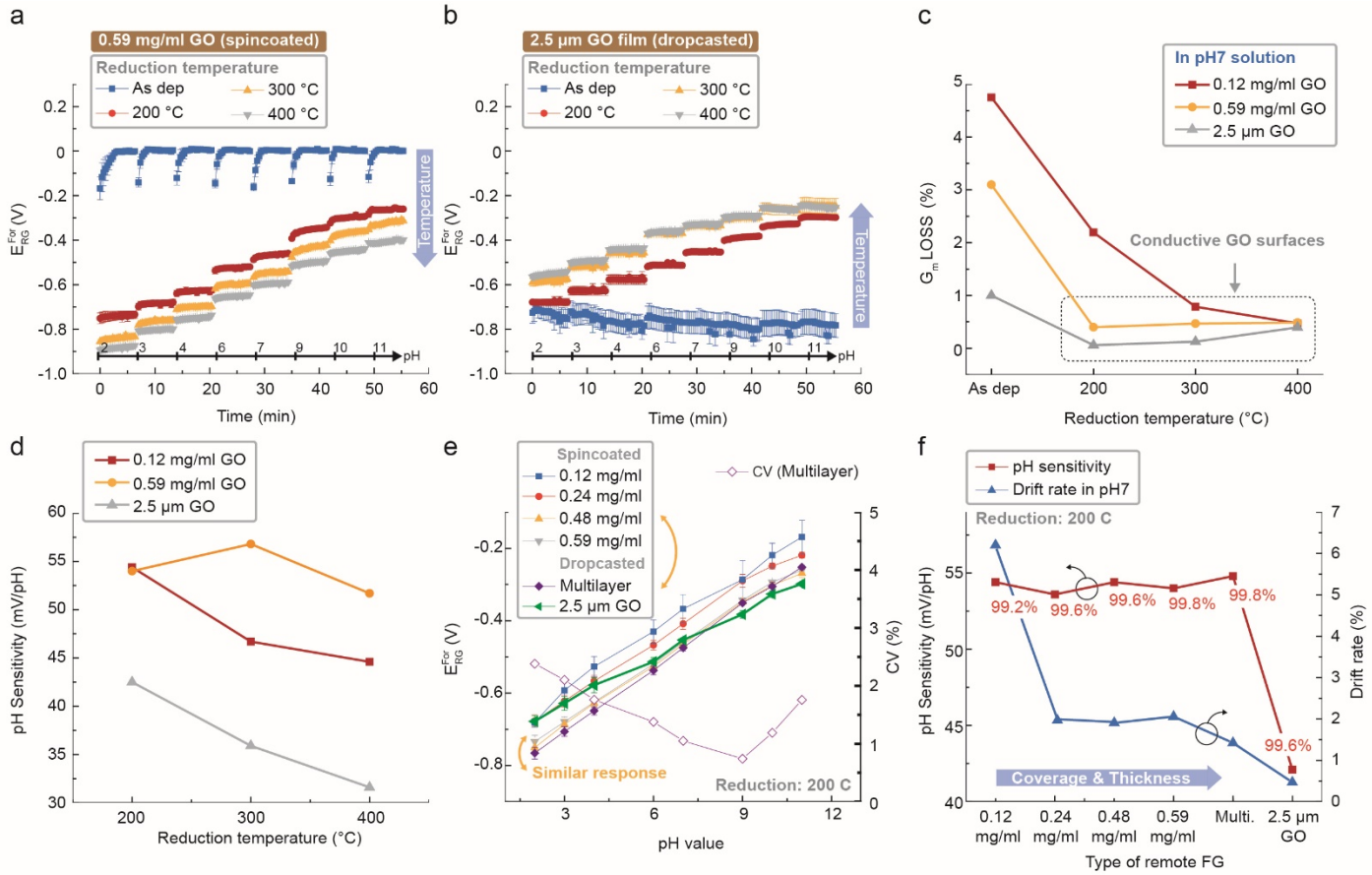
a
0.59 mg/ml GO (spincoated)
Reduction temperature
As dep
300 °C
200 °C
400 °C
Temperature
pH
Time (min)
b
2.5 μm GO film (dropcasted)
Reduction temperature
As dep
300 °C
200 °C
400 °C
Temperature
pH
Time (min)
c
In pH7 solution
0.12 mg/ml GO
0.59 mg/ml GO
2.5 μm GO
Conductive GO surfaces
As dep
Reduction temperature (°C)
d
0.12 mg/ml GO
0.59 mg/ml GO
2.5 μm GO
pH Sensitivity (mV/pH)
Reduction temperature (°C)
e
Spincoated
0.12 mg/ml
0.24 mg/ml
0.48 mg/ml
0.59 mg/ml
Dropcasted
Multilayer
2.5 μm GO
CV (Multilayer)
Similar response
Reduction: 200 C
pH value
f
pH sensitivity
Drift rate in pH7
Reduction: 200 C
99.2%
99.6%
99.6%
99.8%
99.8%
99.6%
Coverage & Thickness
0.12 mg/ml
0.24 mg/ml
0.48 mg/ml
0.59 mg/ml
Multi.
2.5 μm GO
Type of remote FG
Drift rate (%)

Figure 5

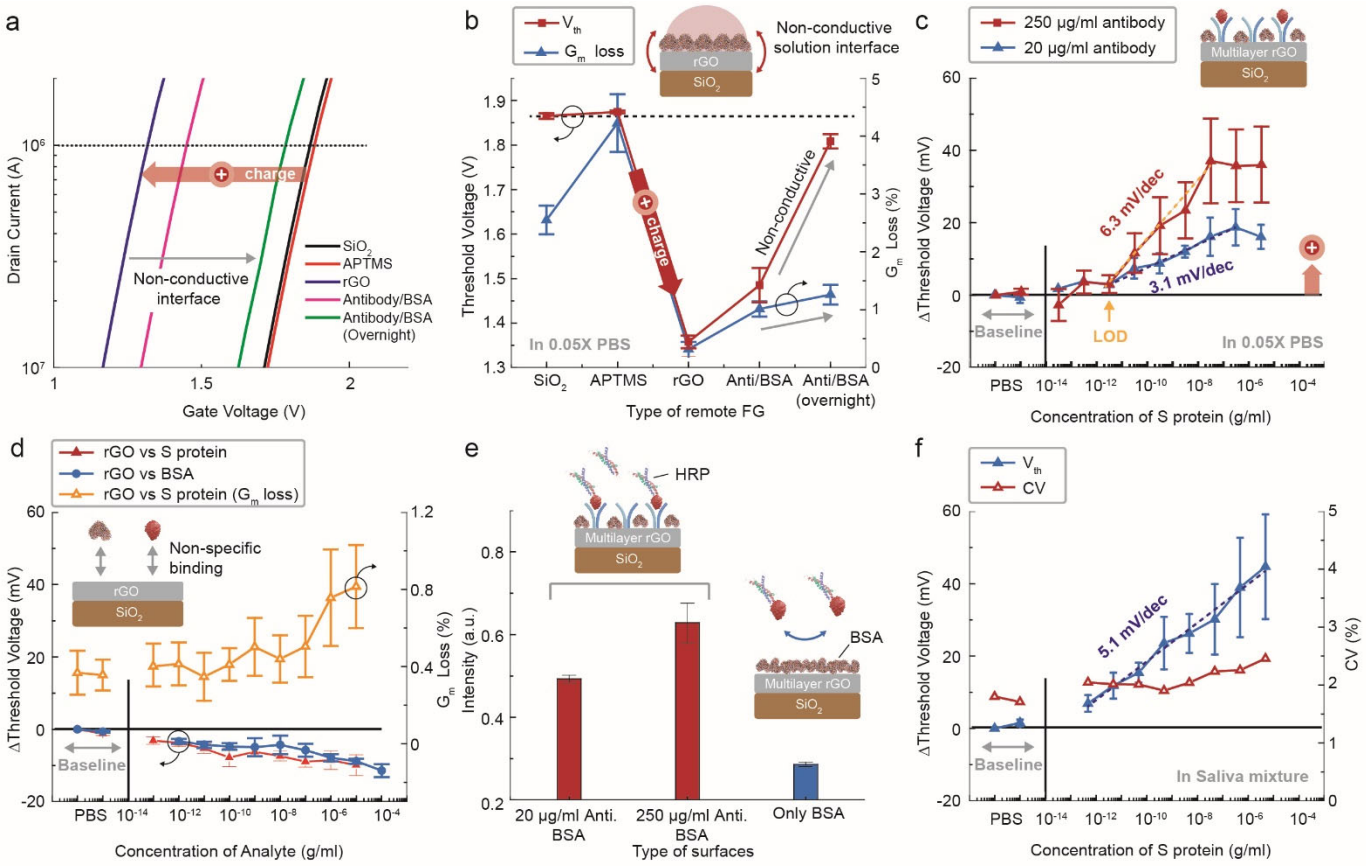
a
Drain Current (A)
Gate Voltage (V)
charge
Non-conductive interface
SiO2
APTMS
rGO
Antibody/BSA
Antibody/BSA (Overnight)
b
Vth
Gm loss
Non-conductive solution interface
rGO
SiO2
Threshold Voltage (V)
Gm Loss (%)
charge
Non-conductive
In 0.05X PBS
SiO2
APTMS
rGO
Anti/BSA
Anti/BSA (overnight)
Type of remote FG
c
250 μg/ml antibody
20 μg/ml antibody
Multilayer rGO
SiO2
ΔThreshold Voltage (mV)
6.3 mV/dec
3.1 mV/dec
Baseline
LOD
In 0.05X PBS
PBS
Concentration of S protein (g/ml)
d
rGO vs S protein
rGO vs BSA
rGO vs S protein (Gm loss)
Non-specific binding
rGO
SiO2
ΔThreshold Voltage (mV)
Gm Loss (%)
Baseline
PBS
Concentration of Analyte (g/ml)
e
HRP
Multilayer rGO
SiO2
BSA
Intensity (a.u.)
20 μg/ml Anti. BSA
250 μg/ml Anti. BSA
Only BSA
Type of surfaces
f
Vth
CV
ΔThreshold Voltage (mV)
CV (%)
5.1 mV/dec
Baseline
In Saliva mixture
PBS
Concentration of S protein (g/ml)

Figure 6

For Table of Contents Only